THE ASTROPHYSICAL JOURNAL, 416:235–246, 1993 October 10

AN *IRAS* SAMPLE FROM CO-ADDED IMAGES OF L1641[1]

H. CHEN[2] AND A. T. TOKUNAGA
Institute for Astronomy, University of Hawaii, 2680 Woodlawn Drive, Honolulu, HI 96822
AND
Y. FUKUI
Department of Astrophysics, Nagoya University, Chikusa-ku, Nagoya 464, Japan
Received 1993 February 11; accepted 1993 April 20

ABSTRACT

A sample of 224 *IRAS* sources was obtained from the *IRAS* co-added images in the dark cloud L1641. Most of these sources were observed in CO and ^{13}CO ($J = 1$–0). The 122 sources within L1641 are likely to be embedded young stellar objects (YSOs). The sources outside L1641 are mostly extended far-infrared cirrus emission. The infrared and millimeter data were used to search for the indicators of the evolutionary state of YSOs. The *IRAS* sources associated with CO outflows are significantly different from the nonoutflow sources because those with CO outflows have higher ^{13}CO column densities, higher far-infrared luminosities, and cooler *IRAS* color temperatures.

Subject headings: infrared: interstellar: continuum — ISM: individual (L1641) — ISM: jets and outflows — ISM: molecules

1. INTRODUCTION

The *Infrared Astronomical Satellite* (*IRAS*) surveyed 95% of the sky in four infrared bands at 12, 25, 60, and 100 μm, and opened new ground in the study of star formation. Many *IRAS* sources are found in active star-forming regions. In a sample of 95 NH_3 dense cores in Taurus, Ophiuchus, and Cygnus detected by Myers & Benson (1983), Beichman et al. (1986) found that nearly 50% of them are associated with *IRAS* sources, and some of them could be "protostellar objects" in the sense that one-half of their luminosity comes from gravitational collapse. In addition, the detection rate of CO outflows in dense cores associated with *IRAS* sources is much higher than in dense cores undetected by *IRAS* (Myers et al. 1988).

In the earlier statistical studies, much attention was drawn to *IRAS* sources that are associated with known star-forming activity, such as molecular dense cores, CO outflows, and T Tauri stars (Beichman et al. 1986). They did not systematically study all the *IRAS* sources in a single molecular cloud, and therefore conclusions on the evolutionary state of the *IRAS* sources were complicated by the different environments and evolutionary histories of the sources. A different approach is to study all the sources within one molecular cloud that are listed in *IRAS* Point Source Catalog (1988; hereafter PSC), such as has been done for L1641 (Strom et al. 1989b) and Taurus (Kenyon et al. 1990). In this type of study, sources at different evolutionary stages will allow us to understand the star-formation process in a larger context. In addition, because all sources are located within a single molecular cloud at a known distance, the analysis is simpler. The availability of *IRAS* co-added images makes it feasible to select an unbiased *IRAS* sample with a sensitivity 2–3 times higher than that of the PSC. The enhanced sensitivity will allow us to detect new sources and to make improved detections for the sources that have only upper limits in the PSC. The recent study of molecular cloud ρ Oph is a good example of such a study (Wilking, Lada, & Young 1989).

To characterize the evolutionary state of young stellar objects (YSOs) in a single molecular cloud, we have undertaken a comprehensive infrared and millimeter study of an unbiased *IRAS* source sample selected from the co-added images in the nearby dark cloud L1641. *Our major goal is to use the IRAS data set and the millimeter observations to understand the nature of the IRAS sources and to find the critical physical parameters that characterize YSOs in L1641.*

L1641 is part of the Ori A molecular cloud at a distance of 480 pc. In contrast to the star-forming activity in the north, i.e., in Orion KL and the Trapezium cluster, L1641 is believed to be a low- and intermediate-mass star-formation region (Cohen & Kuhi 1979). The variety of YSOs and the extensive studies of L1641 make the region suitable for a comparative study at different wavelengths. Herbig & Bell (1988) detected 30 emission-line stars in L1641, most of them T Tauri stars. The most prominent source, NGC 1999, is illuminated by V380 Ori, a possible Ae or Be star (Herbig & Bell 1988). Within the region studied by Strom et al. (1989b) there are 123 sources in the PSC. Many of them have a flat or rising spectral energy distribution, and they are probably embedded YSOs. The entire molecular cloud has been mapped in CO and ^{13}CO (Fukui et al. 1986; Bally et al. 1987). In an unbiased CO $J = 1$–0 emission-line survey, Fukui (1989) discovered eight CO outflows in this region. Several additional outflow candidates were detected later in an *IRAS* flux-limited sample (Morgan & Bally 1991, hereafter MB; Morgan et al. 1991). L1641 has also been extensively studied in X-ray (Strom et al. 1990), in radio continuum emission (Morgan, Snell, & Strom 1990), and in the near-infrared (Strom, Margulis, & Strom 1989a; Chen, Tokunaga, & Hodapp 1991). In § 2, we describe the *IRAS* source selection and flux determination. Three physical parameters (*IRAS* color temperature, far-infrared luminosity, and ^{13}CO column density) of the sources are derived in

[1] The *IRAS* data were obtained using the facilities of Infrared Processing and Analysis Center (IPAC). IPAC is funded by NASA as part of the *IRAS* extended emission program under contract to JPL.

[2] Present address: Harvard-Smithsonian Center for Astrophysics, Mail Stop 42, 60 Garden Street, Cambridge, MA 02138.

§ 3. We discuss the nature of the *IRAS* sources in § 4 by studying the spatial distribution of the sources and their loci in the *IRAS* color-color diagram. In § 5 we examine potential evolutionary indicators of YSOs. The major results are summarized in § 6.

2. SOURCE SELECTION

L1641 was identified by Lynds (1962) as a dark cloud with an optical obscuration level of 4 (approximately $A_V = 4$ mag). Figure 1 shows the ^{13}CO molecular gas distribution of L1641 (Fukui & Mizuno 1991). The lower contour level is 3.0 K km s^{-1}, an approximate 3 σ detection of the ^{13}CO integrated intensity. This contour level gives a ^{13}CO column density of 3×10^{15} cm^{-2} under the typical interstellar conditions ($T_{ex} = 15$ K, $\Delta v = 1.0$ km s^{-1}). This corresponds to a visual extinction of $A_V = 3$ mag using the $N(^{13}\mathrm{CO})$–A_V relationship given by Dickman & Herbst (1990), and it encompasses the dark cloud boundary defined by Lynds. Following Strom et al. (1989b), we focus on the region with R.A. between 5^h30^m and 5^h45^m and declination between $-6°00'$ and $-9°45'$, which covers the entire L1641 cloud, as shown in Figure 1.

2.1. *Source Selection*

The *IRAS* time-ordered data set can be rebinned into a position-ordered data set or a two-dimensional image. Several such images in the same area can be combined into a co-added image with sensitivity 2–3 times higher than that of the PSC. We obtained the co-added images from the Infrared Processing and Analysis Center (IPAC) in two main fields in the four *IRAS* bands. The two images (2°.25 × 2°.25 each) cover the entire L1641 cloud (see Fig. 1), and they are the same regions studied by Strom et al. (1989b). Each image contains 540 × 540 pixels at 12 and 25 μm, 270 × 270 at 60 μm, and 135 × 135 at 100 μm. This yields a scale of 15 arcsec pixel^{-1} at 12 and 25 μm, 30 arcsec pixel^{-1} at 60 μm, and 60 arcsec pixel^{-1} at 100 μm. For comparison, co-added images are also obtained in two nearby areas, also indicated in Figure 1. The scale for the control areas is 30 arcsec pixel^{-1} at all four wavelengths.

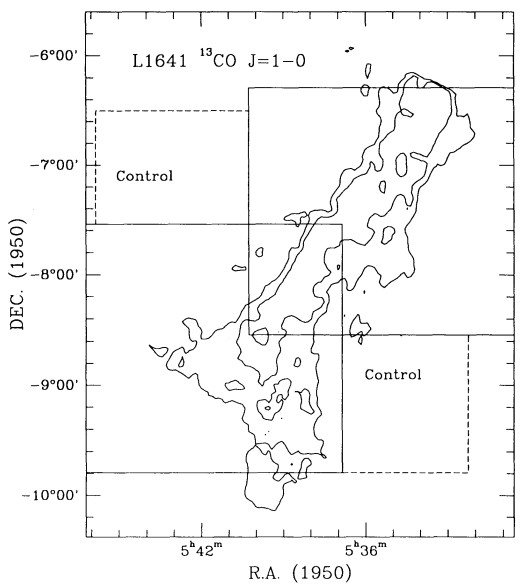

FIG. 1.—The molecular cloud L1641. The contour represents the distribution of the integrated emission of ^{13}CO (the lower contour level is 3.0 K km s^{-1} [Fukui & Mizuno 1991]). The solid boxes show the areas where the main regions of the *IRAS* co-added images are. Two smaller control areas are shown by the dashed boxes.

Three tests were used to select sources from the co-added images (in both main regions and control regions):

1. *Pixel signal-to-noise ratio* (S/N).—The images were divided by their corresponding noise frames, and the pixels with S/N < 3 were rejected.

2. *Source significance.*—Aperture photometry was obtained on the pixels that passed test (1). The aperture on the sources was 3 pixels in diameter, and the annular aperture on the sky was 2 pixels wide around the source aperture. The sources with total flux less than 3 times that of surrounding annular regions were rejected.

3. *Source Positions.*—For that has passed tests (1) and (2), the pixel with the maximum value within 1′ × 1′ box was taken as the source position. Areas that do not have a well-defined peak inside the box were rejected. This process rejected the signal peaks that occurred only in the in-scan direction as a result of ridgelike emission features.

We obtained 312 sources by applying the above three tests to the co-added images at 12, 25, and 60 μm. For sources that were detected at more than two wavelengths, a source was regarded as a single source if its 12 μm and 25 μm positions agree within 30″, or its 12 μm or 25 μm positions at 60 μm positions agree within 1′. The source positions were determined by their peak emission at 12 μm (or 25 μm if there was no detection at 12 μm). These positions were used to determine the source fluxes.

2.2. *Flux Determination*

The *IRAS* fluxes of the sources were determined using the addscan data obtained from IPAC. At each source position, an IPAC program ADDSCAN extracted 10–12 single scans in the in-scan direction, which is approximately the north–south direction in L1641, from the *IRAS* data base. They were combined to construct the addscans in four different ways: simple co-adding (scan code 999), mean of the scans (code 1001), median of the scans (code 1002), and noise-weighted co-adding (code 1003). Of the four addscans, the noise-weighted scan (code 1003) usually has the highest S/N. It is therefore used in most of the cases. The other scans were used only if one of the following problems was encountered with the code 1003: (1) the baseline was bad; (2) spikes appeared in the profile; or (3) adjacent sources affected the scan profile.

The combined scans were then compared to the point source template. For each addscan, an IPAC program SCANPI calculated four flux estimators in each band: the peak value within a given aperture, the integrated flux between the zero points, the integrated flux within the given aperture, and the amplitude of the fitted point source template. To select the appropriate flux estimator, we divided all the sources into pointlike sources and extended sources. The spatial-intensity profiles of the sources were fitted by the point source template to obtain the FWHM of the fitted template, $\langle W50 \rangle$, which was used to describe the angular size of the sources. For this study, sources with $\langle W50 \rangle$ at 12 μm < 1′.1 were classified as the point sources, and those with $\langle W50 \rangle$ > 1′.1 as the extended sources. For sources that seemed to be multiple sources or those not detected at 12 μm, the same classification was carried out at 25 μm. Note this criterion corresponds to a correlation coefficient flag of A, B, C, and D in the PSC. This more restricted criterion allowed us to separate the true point sources from the slightly

extended sources. As will be shown, there are indeed many differences between the point and the extended sources.

Once a source was classified as a point or an extended source, the flux estimator was chosen according to its angular extent. For the point sources, the four estimators described above were usually very consistent with each other, and in most cases, the amplitude of the fitted point source template was assigned to the source flux. For the extended sources, integrated fluxes were chosen. The flux uncertainty was determined by the rms deviation of the residuals after the baseline fitting by SCANPI.

2.3. *Source Sample*

The final selection criterion was that the sources have at least one clear detection at 12, 25, or 60 μm (with an S/N > 5). We excluded sources that can be detected only in the 100 μm band because most of these sources are probably infrared cirrus. Of 312 sources selected from the co-added images, we rejected 73 sources with an S/N < 5 in all three bands to improve the reliability of the detections, one source that is coincident with a galaxy (Strom et al. 1989b), and 14 other sources that are probably foreground or background stars as determined by Strom et al. (1989b). After excluding these sources, we selected 224 sources (98 point sources and 126 extended sources).

The association of the *IRAS* sources with the molecular cloud L1641 was examined. The spatial distribution of all the sources is superposed onto the ^{13}CO contour map of the L1641 in Figure 2. A source is considered to be associated with the molecular cloud if it is located inside the ^{13}CO contour (3.0 K km s^{-1}). Note that most point sources (*filled circles in the left panel*) are located within the contour, while the extended sources (*open circles in the right panel*) are almost randomly distributed. As will be discussed in § 4, most of the sources located outside the molecular cloud are probably either infrared cirrus or foreground stars. While the complete sample of the 224 *IRAS* sources can be found in Chen (1992), Table 1 presents only the 122 sources that are located inside L1641.

2.4. *Comments on the Sample*

1. Of the 123 sources in the *IRAS* PSC (Strom et al. 1989b), 106 are selected following the tests in § 2.1. For the 17 PSC sources that were not detected, three are probably caused by source confusion. The other 14 sources are not associated with a peak of emission; instead they are often located in a ridge that is extended in the cross-scan direction, and five of them are classified as spurious sources by Strom et al. (1989b). In our sample, there are 27 newly detected point sources (15 of them inside the molecular cloud). The average flux density of the newly detected point sources is 0.34 Jy at 12 μm, about a factor of 2 lower than the upper limit of 12 μm flux PSC (0.5 Jy at 3 σ). We attribute these new detections to the enhanced sensitivity of the *IRAS* co-added images.

2. For the 106 PSC sources, we have compared the positions determined from co-added images with the positions given in PSC. The co-added source positions agree with the PSC position well in the in-scan direction, with 77% of the sources having a position difference less than 15″. The position discrepancy is much larger in the cross-scan direction with 75% of the sources having position difference less than 45″. Such a large position discrepancy was also found by Schwartz, Gyuludaghian, & Wilking (1991) in IC 1396. At least two factors may cause the discrepancy: (1) the PSC positions were based on two to three bands, while the co-added position is mainly determined by the 12 μm peak, and (2) the PSC positions were determined by the point source template. If a source is not a well-defined point source, the position will be different from the peak position. The second possibility is supported by the fact that most of the sources that have a large position difference are extended sources.

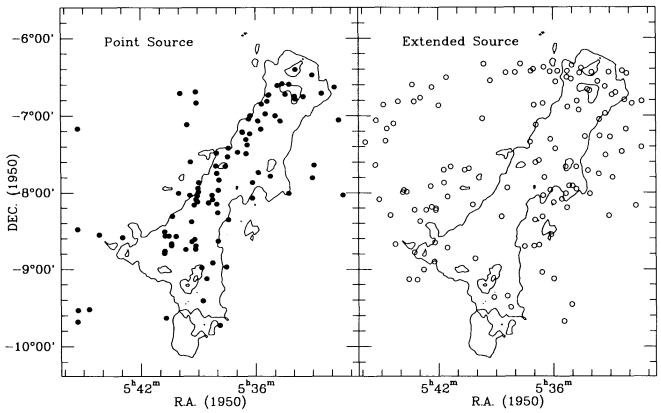

FIG. 2.—*IRAS* sources selected from the co-added images are superposed on the ^{13}CO integrated intensity map. The point sources (*filled circles*) and the extended sources (*open circles*) are shown in the left and right panels, respectively.

3. We have also compared our sample with the sample by MB. The MB sample was selected in a smaller region that corresponds to one of our main fields (the upper right one in Fig. 1). Of 67 sources they listed 51 (76%) were detected in our sample. The other 16 sources are very faint and may contain spurious sources. When comparing the flux densities, the two samples agree well for the point sources. For some extended sources, our flux densities are larger than those in MB, this is probably because we used the integrated flux densities for the extended sources.

4. It is very difficult to draw a uniform detection limit because the noise level varies from source to source and because some sources might be confused by the nearby sources. For the isolated sources, we estimate a 5 σ upper limit of 0.2, 0.2, 0.7, and 7 Jy at 12, 25, 60, and 100 μm, respectively. The flux errors can be as high as 50% in the confused regions, especially in the 60 and 100 μm bands.

5. Although we classified the sources into point and extended types, this classification is subject to source confusion within the *IRAS* beam. We cannot be absolutely certain that all sources classified as point or extended are due to emission from a single source. However, as shown in the next section, many differences between the point sources and the extended sources do indicate that they are different in nature.

6. Our source selection is biased against evolved stars that have relatively little far-infrared emission. Since our major interest is to study the stars in an early evolutionary stage, the above bias is not critical. Of the 30 emission-line stars in the region (Herbig & Bell 1988), 12 of them (40%) have been detected in this study. The sample is also biased against the sources that can be detected only at 100 μm. Most of these sources are likely to be infrared cirrus, although there is a possibility that we might miss extremely young YSOs. We will not discuss these sources in this paper.

TABLE 1

122 *IRAS* SOURCES INSIDE L1641

Number (1)	SN (2)	α(1950) 5^h (3)	δ(1950) (4)	f_{12} (Jy) (5)	f_{25} (Jy) (6)	f_{60} (Jy) (7)	f_{100} (Jy) (8)	T[12, 25] (K) (9)	L_{FIR} ($L_\odot$) (10)	*p-e* (11)	$N(^{13}CO)$ (10^{16} cm^{-2}) (12)	ID (13)	YSO Type (14)	Reference (15)
4	...	35^m 0^s	−6°21′07″	0.37 D	0.57 C	3.9 C	16.1 U	152.5	3.0	e	0.11			
7	4	34 31	−6 23 22	0.6 U	0.65 E	3.7 E	39 F	169.0	11.5	e	1.15			
8	6	33 56	−6 24 07	1.08 D	21.9 A	213 A	601 A	93.6	238	p	5.22	L1641-N	O	1
12	8	35 15	−6 25 37	0.37 D	0.36 D	1.94 E	35 U	171.8	1.8	e	0.13			
17	9	33 04	−6 26 22	3.07 C	5.0 U	22 U	16 U	113.9	7.8	e	1.20			
18	11	33 58	−6 26 37	0.70 D	3.00 D	15.0 C	200 F	118.4	58.5	e	3.77	MSSB-8	O	2
22	...	34 36	−6 27 15	0.2 F	0.33 E	3.0 E	10 F	146.3	4.0	e	0.27			
25	12	33 03	−6 28 37	1.15 A	8.60 A	36.0 A	101 A	110.0	44.3	p	2.52	V801 Ori	T	3
26	...	35 17	−6 30 22	1.31 C	2.16 A	10.8 B	18 E	150.0	11.4	e	0.19			
27	13	35 03	−6 31 52	0.73 E	0.90 D	6.2 E	43 U	161.3	5.0	e	0.20			
29	...	33 39	−6 33 37	3.92 A	4.88 A	26.5 B	57.4 C	160.9	32.2	e	2.61			
30	...	35 52	−6 33 52	1.28 C	1.26 D	6.3 C	12 H	188.6	7.8	e	0.00			
31	16	34 37	−6 35 07	1.07 B	1.07 B	4.9 U	37 U	170.5	2.8	p	1.60	BE Ori	T	3
32	17	34 15	−6 35 37	0.33 A	0.76 B	4.8 U	110 U	155.9	1.3	p	1.04	V846 Ori		4
33	18	34 52	−6 36 37	1.06 C	1.07 D	4.0 F	20 F	170.1	8.6	p	0.63	BF Ori	T	3
34	19	33 16	−6 37 37	0.22 F	0.36 D	6.8 D	18 U	170.5	4.2	e	1.30			
36	22	34 11	−6 39 52	5.58 A	6.05 B	18.0 C	120 D	166.8	48.4	e	0.53	MSSB-18	O	2
37	23	34 04	−6 40 37	5.87 A	8.12 A	13.2 E	192 U	156.6	20.7	e	0.99			
39	25	32 42	−6 42 15	0.30 D	0.32 E	3.0 C	37 U	167.5	2.3	e	0.64			
41	...	32 32	−6 42 37	0.24 D	0.3 C	2.47 B	11 H	142.0	4.2	p	0.65			
42	26	34 27	−6 43 22	0.40 F	0.9 F	7.6 G	32.0 D	155.3	11.8	p	1.01			
44	...	32 54	−6 43 52	1.14 B	1.56 B	5.7 B	11.8 F	157.0	7.5	e	0.43			
46	27	35 20	−6 44 07	2.10 A	2.92 A	5.0 D	20.2 D	156.4	11.7	p	0.27	HD 37357		4
47	28	33 58	−6 44 37	8.58 B	7.35 C	27.0 C	150 U	178.0	31.9	p	3.92	V380 Ori	OA	1, 3
49	30	33 30	−6 45 07	0.96 B	1.94 B	29.7 A	155 B	143.0	51.9	p	2.93			
50	31	33 58	−6 46 22	1.80 C	10.0 H	60.0 B	280 B	116.1	99.6	p	4.90			
51	32	33 56	−6 47 07	0.70 D	5.00 E	80.7 C	262 A	110.9	97.5	p	4.66	MSSB-21	O	2
53	...	34 44	−6 48 45	2.40 B	3.98 A	9.2 D	37.8 U	149.8	10.9	e	0.63			
56	33	35 24	−6 48 52	0.38 U	0.59 C	3.13 C	14.6 U	152.2	2.0	p	0.83			
62	34	35 41	−6 50 52	2.82 A	3.11 A	7.1 B	55.9 A	166.1	22.6	p	0.99			
65	...	35 14	−6 53 15	0.85 U	0.85 U	5.3 C	10.0 D	170.5	4.3	e	0.14			
68	...	34 38	−6 55 45	1.70 A	2.37 A	7.4 D	23.3 U	156.3	7.9	e	0.46			
70	...	33 15	−6 58 22	0.34 E	1.1 F	8.3 A	56.0 B	147.0	18.1	e	0.21			
71	35	35 29	−6 58 22	0.24 U	0.51 C	5.3 C	12 H	141.4	5.1	p	1.75	T456		4
72	37	34 59	−6 59 52	0.74 C	1.34 B	2.4 D	34 U	146.7	3.2	p	1.64			
73	36	36 16	−6 59 52	2.14 B	5.31 A	20.5 A	44.7 B	136.6	24.5	p	0.46			
75	39	36 21	−7 02 22	0.57 C	5.34 A	26.1 A	107 E	105.8	39.8	p	1.96	L1641-C	O	1
78	...	34 43	−7 03 52	0.38 E	0.36 H	4.3 H	7.3 U	154.2	1.0	p	1.47			
79	40	35 53	−7 03 52	53.7 A	124 A	169 A	127 A	138.6	241	p	1.02	V883 Ori	E	3
81	...	36 54	−7 07 15	0.51 U	0.39 U	4.5 B	29.6 C	184.0	9.0	e	0.59			
83	42	35 44	−7 10 07	0.39 E	0.98 B	4.0 C	21.0 U	136.2	3.3	p	2.25	Haro 14a		4
85	44	36 42	−7 12 07	0.5 D	3.11 A	9.6 C	20 H	116.1	10.8	p	0.87			

TABLE 1—*Continued*

Number (1)	SN (2)	α(1950) 5^h (3)	δ(1950) (4)	f_{12} (Jy) (5)	f_{25} (Jy) (6)	f_{60} (Jy) (7)	f_{100} (Jy) (8)	T[12, 25] (K) (9)	L_{FIR} ($L_\odot$) (10)	*p-e* (11)	$N(^{13}CO)$ (10^{16} cm^{-2}) (12)	ID (13)	YSO Type (14)	Reference (15)
87.....	*	36 41	−7 12 37	0.49 C	2.93 A	9.6 C	18 H	114.1	10.2	p	0.80			
89.....	47	36 18	−7 14 07	2.22 B	3.18 B	3.1 C	44.1 U	155.2	6.9	p	0.66	Haro 2-249	T	1
91.....	...	34 19	−7 16 22	0.21 U	0.43 D	1.3 E	11.8 E	142.6	3.7	e	0.85			
95.....	49	36 30	−7 18 07	1.05 B	3.57 B	9.8 B	46.0 U	127.8	8.9	p	0.33	V599 Ori		4
96.....	...	36 08	−7 18 22	0.89 B	1.42 A	8.3 B	23.4 C	151.2	10.9	e	1.36			
97.....	...	37 12	−7 20 22	0.29 D	0.31 D	2.0 E	15.2 E	167.4	5.1	e	0.75			
99.....	51	36 26	−7 22 37	0.79 D	1.43 C	5.3 C	18 H	146.7	8.4	p	1.75			
101.....	52	37 25	−7 24 52	0.54 U	0.50 E	3.9 U	15.1 U	174.2	0.5	p	1.20			
102.....	...	35 53	−7 25 37	0.88 B	1.28 A	4.8 B	6.1 U	154.7	4.7	e	0.73			
104.....	54	36 56	−7 28 07	0.89 B	4.62 A	68.1 A	123 B	117.6	58.2	p	1.83	H4-255	OT	1, 3
105.....	55	38 02	−7 28 52	29.6 A	88.5 A	182 A	219 A	131.2	212	p	1.40	L1641-S	OE	1, 3
106.....	57	36 29	−7 29 07	0.45 U	0.45 D	1.5 U	39.4 U	170.5	0.5	p	1.26			
108.....	59	37 27	−7 31 37	0.30 U	8.99 A	129 A	220 A	88.4	104	p	1.60	L1641.S3	O	1
113.....	61	36 44	−7 34 52	1.54 A	2.17 A	6.2 B	14.1 E	155.9	9.2	e	0.50			
116.....	...	36 55	−7 36 22	0.78 B	1.76 A	5.8 B	11.5 D	139.5	7.1	e	0.59			
119.....	62	38 04	−7 38 52	0.11 U	0.78 B	2.0 D	18.4 U	111.1	1.5	p	1.38			
120.....	63	37 34	−7 39 07	0.45 D	0.81 C	1.4 U	24.7 U	146.9	1.5	p	0.76			
123.....	...	35 20	−7 39 45	0.74 B	0.84 B	4.7 B	21.6 C	164.8	8.7	e	0.20			
124.....	...	34 46	−7 39 52	0.34 D	0.22 U	1.2 U	6.9 U	193.5	0.9	p	0.54			
133.....	...	35 52	−7 44 07	0.2 U	0.57 C	3.0 C	11 D	140.1	4.1	e	0.53			
134.....	67	38 01	−7 44 37	0.2 U	0.43 D	2.1 D	10 U	139.4	1.4	p	1.30			
138.....	...	35 15	−7 46 52	0.7 D	1.33 B	1.96 C	15.6 U	144.0	2.9	e	0.41			
142.....	...	36 28	−7 48 07	0.48 B	0.50 C	4.7 A	37.1 C	168.6	12.0	e	0.49			
146.....	68	37 55	−7 49 52	0.98 B	3.87 A	9.7 B	9.5 U	124.0	8.9	p	1.22			
149.....	69	36 11	−7 51 52	0.13 C	0.31 C	1.5 D	9.6 U	137.8	1.2	p	0.20	Haro 7-1	T	3
150.....	70	38 58	−7 51 52	0.18 C	0.60 C	1.0 E	38.7 U	128.3	1.2	p	1.07			
154.....	...	35 10	−7 54 37	0.59 C	0.67 D	1.65 E	15.0 F	164.8	5.6	e	0.56			
158.....	...	38 24	−7 56 15	0.2 U	0.26 U	1.1 D	7.0 U	152.8	0.6	p	1.18			
160.....	72	39 01	−7 56 22	0.37 B	3.44 B	13.1 A	30.9 E	105.9	14.8	p	1.23			
161.....	...	34 46	−7 57 22	0.18 U	0.32 E	2.2 C	37 C	163.6	10.3	e	0.39			
162.....	...	36 09	−7 57 52	0.90 B	0.42 D	0.6 H	1.9 U	215.3	1.9	e	0.16			
163.....	73	37 57	−7 57 52	0.96 B	2.48 A	5.6 A	16.2 E	135.4	8.9	p	0.90			
168.....	74	38 59	−7 59 22	0.36 C	0.95 A	3.5 U	32.5 U	134.8	1.5	p	1.42			
171.....	76	40 02	−8 00 07	0.48 C	0.98 B	2.08 D	20 U	142.7	2.4	p	0.10			
172.....	...	34 17	−8 00 22	0.20 D	0.21 C	0.7 D	10.0 U	168.2	0.8	p	0.17			
173.....	...	35 20	−8 00 37	0.21 D	0.20 E	2.1 D	8.1 F	172.8	3.2	e	0.40			
177.....	78	38 16	−8 01 52	0.2 U	0.32 C	1.9 D	10.0 U	149.2	1.2	p	1.43			
178.....	77	39 26	−8 01 52	0.80 B	1.69 B	4.9 A	10.0 U	141.6	4.8	p	0.93	Haro 7.2	T	3
180.....	...	36 32	−8 02 15	0.4 U	0.3 U	7.8 B	52.0 B	182.9	15.8	e	0.35			
181.....	79	39 03	−8 02 22	0.2 U	0.41 C	2.8 U	28.7 U	133.7	0.4	p	1.15			
186.....	81	39 07	−8 05 07	0.89 B	3.18 B	8.2 D	8.7 U	126.5	7.6	p	1.35			
187.....	82	38 15	−8 08 22	2.09 A	4.72 A	3.0 H	13.2 U	139.5	7.5	p	1.07			
191.....	83	39 02	−8 07 07	1.87 A	3.62 A	6.0 C	7.0 U	144.4	8.1	p	1.59	DL Ori	T	3

TABLE 1—*Continued*

Number (1)	SN (2)	α(1950) 5^h (3)	δ(1950) (4)	f_{12} (Jy) (5)	f_{25} (Jy) (6)	f_{60} (Jy) (7)	f_{100} (Jy) (8)	T[12, 25] (K) (9)	L_{FIR} ($L_\odot$) (10)	*p-e* (11)	$N(^{13}CO)$ (10^{16} cm^{-2}) (12)	ID (13)	YSO Type (14)	Reference (15)
193.....	...	38 27	−8 07 37	0.57 D	2.19 D	15 H	25 H	153.6	13.5	p	1.52			
194.....	85	38 27	−8 08 07	0.60 D	1.80 D	12 H	20 H	129.0	11.1	p	1.37	L1641-S4	O	1
196.....	86	38 01	−8 08 52	0.4 B	0.6 B	0.78 C	28 U	159.7	1.4	p	0.70	Haro 7-4	T	3
198.....	87	39 12	−8 09 37	0.27 C	1.34 C	2.2 C	11.2 E	143.8	4.7	p	1.56			
211.....	91	37 58	−8 15 37	0.46 B	1.14 A	2.7 C	8.4 E	136.6	4.4	p	0.68			
216.....	93	40 22	−8 18 22	0.94 B	4.41 A	15.1 B	50.0 F	119.9	21.7	p	0.42	L1641-S2	O	1
217.....	...	38 42	−8 18 45	0.21 U	0.40 B	1.6 B	3.4 D	145.0	1.6	e	0.91			
224.....	94	39 21	−8 22 52	0.37 C	0.62 B	1.0 D	10.5 U	149.4	1.5	p	0.91			
228.....	...	45 19	−8 28 52	0.13 E	0.10 U	0.28 D	9.1 U	183.7	0.4	p	0.00			
229.....	95	40 46	−8 30 37	0.13 F	0.52 B	1.1 E	5.4 U	119.7	1.1	p	0.29			
232.....	98	40 33	−8 33 52	0.24 U	0.48 D	1.6 D	2.4 H	143.3	1.4	p	0.30			
233.....	...	40 44	−8 33 52	0.17 U	0.19 E	0.8 U	5.0 U	165.5	0.2	p	0.20			
234.....	97	40 10	−8 34 07	0.16 U	0.23 D	1.0 C	11.3 E	155.1	3.3	p	0.54			
235.....	...	42 58	−8 35 07	0.21 D	0.21 U	1.1 U	23.8 U	170.5	0.5	p	0.29			
237.....	99	39 11	−8 36 37	0.40 C	1.97 A	5.3 B	15 H	118.8	7.3	p	0.62			
240.....	100	39 19	−8 38 22	0.35 B	0.50 E	0.5 U	7.3 U	155.4	1.1	p	0.63			
242.....	...	42 11	−8 39 07	0.09 E	0.35 E	0.2 U	8.0 U	154.9	0.4	e	0.32			
243.....	101	40 24	−8 39 52	0.80 A	1.20 E	1.4 E	10 H	153.5	4.9	p	0.95			
245.....	103	40 24	−8 41 22	0.70 A	1.33 A	1.9 B	10 H	150.1	5.0	p	0.99			
246.....	104	39 07	−8 41 37	0.26 D	0.73 B	3.5 B	16.8 B	133.0	6.2	p	0.70			
250.....	...	41 31	−8 43 22	0.12 U	0.2	0.48 E	17 F	170.5	4.5	e	0.48			
251.....	105	39 08	−8 44 22	0.22 U	0.99 B	4.1 C	19.6 U	120.8	2.8	p	0.48			
252.....	...	39 39	−8 44 37	0.28 C	0.17 U	0.8 U	10.3 U	197.4	0.7	p	0.43			
256.....	106	40 45	−8 45 37	0.17 U	0.77 B	4.0 B	15.5 A	165.5	5.7	p	0.97			
257.....	...	43 15	−8 46 52	0.12 U	0.14 U	0.7 C	4.6 H	163.6	1.4	e	0.19			
258.....	107	40 46	−8 47 22	0.14 U	0.40 B	3.2 D	15.8 D	132.5	5.3	p	0.16			
261.....	...	40 05	−8 51 45	0.16 U	0.12 U	0.4 D	6.9 E	185.0	1.9	e	0.64			
264.....	108	38 15	−8 54 45	0.16 E	0.22 E	1.5 C	6.8 A	156.8	2.6	p	0.00			
266.....	110	37 32	−8 58 07	0.41 C	0.2 H	0.7 U	7.7 U	215.9	0.8	p	0.10			
267.....	111	38 49	−8 58 45	0.10 U	0.36 B	6.2 A	7.8 D	126.3	4.3	p	0.34			
270.....	113	38 33	−9 07 22	0.95 B	2.14 A	1.9 D	8.3 E	139.5	5.4	p	0.64			
276.....	114	38 23	−9 20 52	6.15 F	10.0 U	30.0 E	185 F	150.5	72.0	e	0.42			
277.....	116	39 05	−9 21 45	0.99 B	1.71 A	5.9 C	86.9 A	148.3	26.5	e	0.44			
280.....	118	38 44	−9 24 37	0.79 B	3.04 A	19.1 B	40 E	124.6	19.5	p	0.09			
281.....	119	38 13	−9 29 37	1.71 B	1.47 B	7.5 U	105 U	117.8	4.2	e	0.34			
288.....	123	37 52	−9 43 37	0.88 A	1.70 A	1.2 D	9.0 U	144.5	2.9	p	0.19	V350 Ori	T	3
289.....	...	40 27	−9 46 22	0.2 D	0.5 D	0.5 U	6.7 U	143.3	0.8	p	0.48			

NOTES.—Col. (1) gives the source number. Col. (2) is the corresponding number assigned by Strom et al. (1989b). Cols. (3) and (4) are the coordinates of the sources at 1950 epoch. Cols. (5)–(8) are the source fluxes at 12, 25, 60, and 100 μm, respectively. If there is no detection, a 5 σ upper limit is given with a flag U. The uncertainty of the flux densities are flagged in the following convention: A, 4%; B, 4%–8%; C, 8%–12%; D, 12%–16%; E, 16%–20%; F, 20%–50%; G, 50%; and H, 100%. Col. (9) is the color temperature derived from *IRAS* 12 and 25 μm flux ratio. Col. (10) is the far-infrared luminosity integrated from 7 μm to infinity in solar units. Col. (11) indicates source type: p for point source and e for extended source. Col. (12) gives the ^{13}CO column density toward the source. Col. (13) gives source identification from Strom et al. (1989b). Col. (14) shows if the source is a known YSO: O for outflow, A for Ae or Be star, T for T Tauri star and E for emission-line star. Col. (15) gives references as follows: (1) Fukui 1989; (2) Morgan et al. 1991; (3) Herbig & Bell 1988; and (4) Strom et al. 1989b.

3. THE PHYSICAL PROPERTIES

3.1. *Color Temperature*

If cold dust is in thermal equilibrium and its emissivity is proportional to ν^n, a color temperature between two wavelengths λ_1 and λ_2 can be calculated as

$$T[\lambda_1, \lambda_2] = \frac{hc}{k}\left(\frac{1}{\lambda_2} - \frac{1}{\lambda_1}\right)\Big/\ln\frac{F(\lambda_1)}{F(\lambda_2)} + (n+3)\ln\frac{\lambda_1}{\lambda_2}\ \mathrm{K}\ , \quad (1)$$

where $F(\lambda_1)$ and $F(\lambda_2)$ are the source flux densities at wavelengths λ_1 and λ_2, and h, c, and k are the Planck constant, the speed of light, and Boltzmann constant, respectively (Emerson 1988a). For the dust emissivity dependence on frequency, we adopt the result of Draine & Lee (1984) that gives $n = 2$ for both graphite and silicate. As will be discussed in the next section, the far-infrared emission of the *IRAS* sources located inside L1641 is mostly thermal emission, and equation (1) can be applied. For each of these sources, a color temperature, $T[12, 25]$, is obtained using the 12 and 25 μm flux ratio and is listed in Table 1. Equation (1) may not be valid for the sources located outside of L1641, because their emission at 12 and 25 μm is probably dominated by the nonthermal emission from very small grains (VSGs) heated by the interstellar UV photons.

3.2. *Far-Infrared Luminosity*

Given the *IRAS* flux densities in the four *IRAS* bands, and assuming that the dust emission spectrum F_λ is proportional to λ, the source infrared luminosity between 7 and 135 μm can be calculated as

$$L = 3.2 \times 10^{-5} D^2 (20.65 f_{12} + 7.54 f_{25} + 4.68 f_{60} + 1.76 f_{100})(L_\odot)\ , \quad (2)$$

where D is the distance to the source in parsecs, and F_λ is the flux density in Jy at λ (Emerson 1988b). To account for the luminosity beyond the observable bands, we use a method suggested by Myers et al. (1987). Assuming that blackbody radiation peaked at the longest observable wavelength $\lambda_{\max}$ with flux density $F_{\max}$, the luminosity longward of $\lambda_{\max}$ can be written as

$$\Delta L = 5.33 \times 10^{-5} D^2 (F_{\max})/\lambda_{\max}\ (L_\odot)\ . \quad (3)$$

The total far-infrared luminosity of the *IRAS* sources, $L_{\mathrm{FIR}} = L + \Delta L$, is given in Table 1.

3.3. ^{13}CO *Column Density*

We made CO and ^{13}CO millimeter observations to determine the gas column density toward the *IRAS* sources. The CO ($J = 1$–0) and ^{13}CO ($J = 1$–0) line emission at 115 and 110 GHz were observed using the Nagoya University 4 m millimeter telescope on 1990 March 26–27. The telescope has a beam size of 2.7. A 4 K SIS receiver was used, and the system temperature was about 400 K (double-sided band). For each of the *IRAS* sources selected in the two main fields, a single-point observation was made at the *IRAS* position. Ori A was observed during the observations for the temperature calibration. The rms noise was typically 1.0 K and 0.35 K for CO and ^{13}CO, respectively.

The data reduction was carried out using the Nagoya data reduction system. After the baseline removal, a Gaussian fit to the line profile gave three parameters: the peak temperature, the line width, and the line center. Using these parameters we estimated the ^{13}CO column density toward each *IRAS* source. The CO line is usually optically thick so that the CO antenna temperature gives a direct measurement of the gas excitation temperature. With the assumptions that both CO and ^{13}CO are in thermal equilibrium with the same excitation temperature, ^{13}CO line is optically thin, and the line profile is Gaussian, we calculate the ^{13}CO column density from (Scoville et al. 1986)

$$N(^{13}\mathrm{CO}) = 2.49 \times 10^{14}\ \frac{(T_{\mathrm{ex}} + 9.2)\tau_0\,\Delta v}{1 - \exp\,(-5.31/T_{\mathrm{ex}})}\ \mathrm{cm}^{-2}\ , \quad (4)$$

where Δv is the ^{13}CO line width (FWHM), and the excitation temperature of CO and ^{13}CO gas, T_{ex}, can be determined by $T(^{12}\mathrm{CO})$. The optical depth at line center, τ_0, can be obtained by using the peak temperatures of CO and ^{13}CO and assuming $X(\mathrm{CO})/X(^{13}\mathrm{CO}) = 89$. Note that for $T_{\mathrm{ex}} = 20$ K, the ^{13}CO line will become optically thick ($\tau_0 > 1$) when the column density reaches 2×10^{16} cm^{-2}, and the ^{13}CO line will not be a good measure of the gas density at the center of some molecular dense cores. The ^{13}CO column density $N(^{13}\mathrm{CO})$ of the *IRAS* sources is presented in Table 1.

4. THE NATURE OF THE SOURCES

4.1. *Point Sources versus Extended Sources*

Figure 2 shows the spatial distribution of the point sources and the extended sources in L1641. The point sources are clearly associated with the molecular cloud (as defined by the ^{13}CO integrated intensity contour map), and 81% of them are located inside the molecular cloud. On the other hand, the distribution of the extended sources appears to be random, and only 37% of the extended sources are located inside the L1461 boundary. Table 2 shows the association of the sources with the L1641. Using the contingency table statistical test, we find that the distributions of the point sources and the extended sources are different at a much greater than 99.9% level of confidence.

The color-color diagram using *IRAS* fluxes at 12, 25, and 60 μm is often used for the first-order classification of the *IRAS* sources (Beichman 1985; Emerson 1988b). We plotted the point sources and the extended sources in Figures 3*a* and 3*b*, respectively. It is clear that the point sources and the extended sources are distributed differently in the color-color diagrams. Most of the point sources are spread widely across the diagram, and 50% of them are located inside the boxes defined by known T Tauri stars and molecular dense cores. In contrast, almost all the extended sources are located in a region appropriate for hot cirrus as defined by Beichman (1985). These results, together with the concentration of the point sources within the molecular cloud, suggest that most of the point sources are probably YSOs and most of the extended sources are not.

TABLE 2

SPATIAL DISTRIBUTIONS OF THE SOURCES

Parameter	Point Source	Extended Source	Total
Inside L1641	79	43	122
Outside L1641	19	83	102
Total	98	126	224

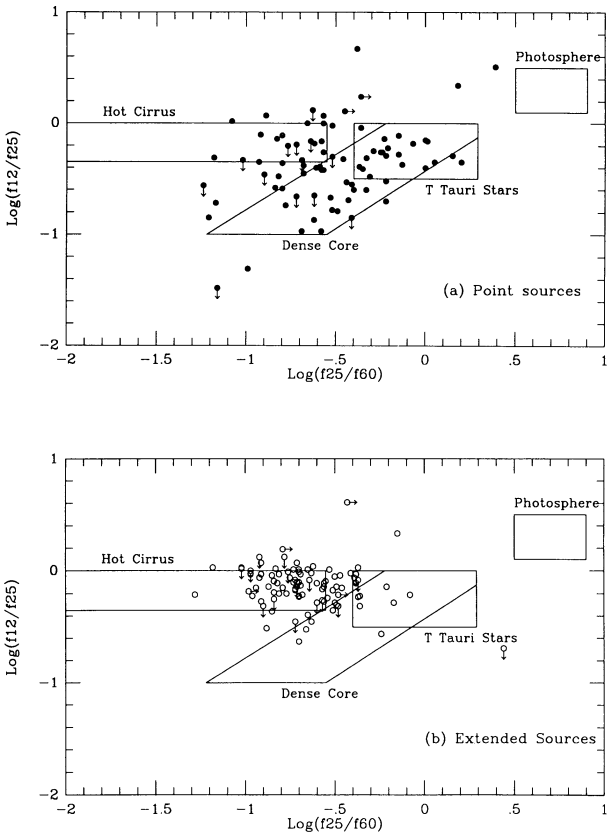

FIG. 3.—The *IRAS* color-color diagram based on 12–25–60 μm fluxes. All the sample sources that have at least two detections (S/N > 5.0) at 12, 25, and 60 μm are plotted. Diagram (*a*) is for the point sources, and (*b*) is for the extended sources. The arrows denote the sources that have no detection at 12 μm (*vertical arrows*) or at 25 μm (*horizontal arrows*). Following Beichman (1985), areas that are often occupied by various types of sources are indicated.

4.2. *Emission Mechanism of the Dust*

The location of the *IRAS* sources in the color-color diagram provides some insights into dust emission mechanisms. The point sources are spread widely in the diagram, indicating a large range of dust temperature. This can be understood if the heating sources are embedded central sources whose temperature varies from source to source, depending on the luminosity of the sources, the dust properties (particle size and composition), and the spatial distributions of the surrounding material.

On the other hand, the extended sources are located in a small region of the color-color diagram that is characteristic of hot cirrus emission. The cirrus emission is thought to arise from the nonthermal emission from VSGs that are heated by UV photons in the interstellar radiation field (Boulanger et al. 1988). Since the VSGs have very small size ($\sim$10 Å) and heat capacity, they can attain a temperature up to 1000 K when heated by a single UV photon. With this stochastic heating and cooling, the VSGs cannot be in thermal equilibrium (Sellgren 1985). The high temperature of the VSGs causes them to dominate the emission at both 12 and 25 μm. The ratio of the two fluxes is therefore insensitive to the thermal equilibrium temperature. The hot VSGs have little emission at longer wavelengths at which the thermal emission from the colder larger grains dominates. Figures 4*a* and 4*b* show the 12–25 μm versus 60–100 μm color-color diagrams of the sources inside and outside the L1641, respectively. In Figure 4*b*, the sources located outside L1641 (most of them are extended) vary by a factor of greater than 10 in the 60–100 μm flux ratio, while their 12–25 μm flux ratio changes only by a factor of 2.

For the large-scale *IRAS* emission in the California nebula, Boulanger et al. (1988) developed an analytical model for VSG emission. Assuming that the far-infrared emission comes from a mixture of the VSGs ($\sim$10 Å) and the larger grains ($\sim$0.5 μm) heated by the interstellar radiation field, they calculated the

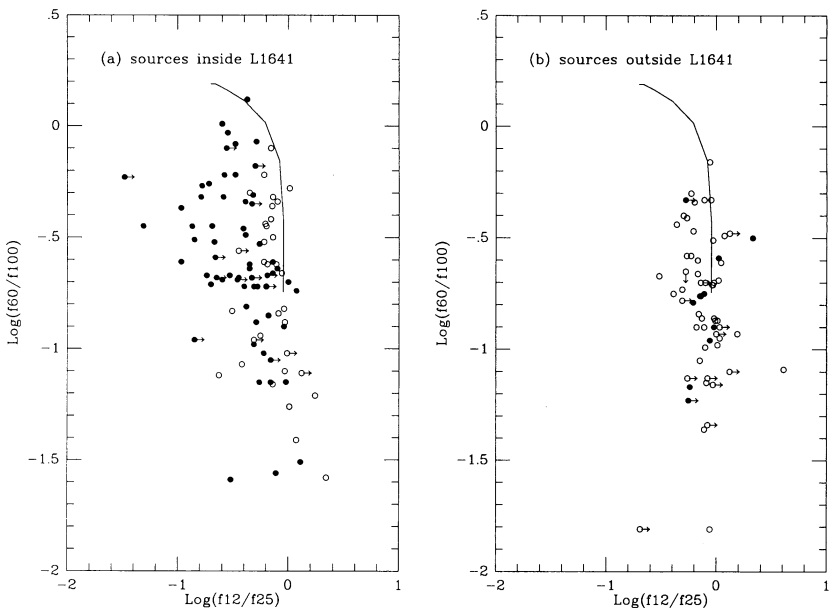

FIG. 4.—The *IRAS* color-color diagram based on 12–25–60–100 μm fluxes. The sources located inside and outside L1641 are plotted in the left and right panels, respectively. The point sources are filled circles, and the extended sources are open circles. The solid curve gives expected *IRAS* colors by the Boulanger et al. (1988) analytical model for the small grain emission.

IRAS colors as a function of equilibrium temperature of the large grains (T_{eq}). As shown in Figure 4*b*, the theoretical calculation (*solid line*) matches our observations very well.

The same analysis was carried out for the sources inside L1641 (most of them are point sources). As shown in Figure 4*a*, most of these sources have the 12–25 μm flux ratio lower than what the model predicted (*solid line*). This indicates that the thermal emission from the large grains dominates over the nonthermal emission from the VSGs. The probable heating sources are the embedded YSOs.

In summary, the source spatial distribution and the *IRAS* color-color diagram show that the sources inside and outside L1641 are significantly different. The sources inside are within the molecular cloud and are probably YSOs, while the sources outside have a spatial distribution and *IRAS* color typical of infrared cirrus. The following discussion will concentrate on the sources located inside L1641, i.e., the 122 sources presented in Table 1.

5. DISCUSSION

The far-infrared emission from a YSO may arise from the central object, a disk system, and a dust shell with a range of temperature. The spectral energy distribution of the YSO may not be fitted by a single-temperature blackbody, and it is therefore difficult to place it in the luminosity-temperature diagram. Using his protostar model, Adams (1990) attempted to use a $L - A_V$ diagram to determine the evolutionary state of a YSO by placing it in a luminosity-visual extinction diagram. Because of light scattering and possible IR excess of YSOs, it is very difficult to determine the extinction in the near-infrared (1–5 μm) and to compare the observations with the model. This motivates us to look for other accessible observational parameters to characterize YSOs. In the following, we use the sample in Table 1 to discuss possible evolutionary indicators. For simplicity we divide the sources in Table 1 into three groups: (1) *outflow sources*, the 11 *IRAS* sources known to be associated with CO outflow; (2) *T Tauri stars*, the nine sources associated with known T Tauri stars; and (3) *other sources*, those not associated with known CO outflow or T Tauri stars.

5.1. $N(^{13}CO)$ *as an Evolutionary Indicator*

The ^{13}CO column density measures the number of ^{13}CO molecules in the line of sight if the emission line $J = 1–0$ is optically thin. Figure 5*a* shows the histograms of $N(^{13}CO)$ for the three groups. Seven of 11 (73%) outflow sources have $N(^{13}CO) > 1.1 \times 10^{16} cm^{-2}$, while only 27 of 111 (24%) nonoutflow sources have $N(^{13}CO)$ higher than that value. To see if the high column density toward the outflow sources is due to a local enhancement associated with the *IRAS* source or just a chance overlap, we made two observations: First, by mapping a group of the *IRAS* sources in ^{13}CO, Chen, Fukui, & Iwata (1993) found that six of eight outflow sources are located inside dense cores, compared with only five of 32 nonoutflow sources. Second, high-angular resolution HCO^+ and ^{13}CO observations with about a 20″ beam size show that the column densities of these two molecules are correlated with each other, and both column densities are well correlated with the *IRAS* colors (Chen, Fukui, & Yang 1992). This indicates that the molecular gas is physically associated with the *IRAS* sources. It is possible that $N(^{13}CO)$ may underestimate the gas column density if the ^{13}CO $J = 1–0$ line becomes saturated. However, because Figure 5*a* shows that outflow sources are usually associated with higher $N(^{13}CO)$ than the nonoutflow sources and are therefore more likely to be saturated, the line saturation should not change the general trend in Figure 5*a*.

The close association of CO outflows with molecular dense gas was previously noticed by Myers et al. (1988) and Morgan & Bally (1991). It indicates that the outflow sources are YSOs still embedded in their parental dense cores. This is expected if stars are indeed formed in dense cores and the outflow characterizes the early stage of star formation. Consequently, the *IRAS* sources associated with less dense gas are statistically more evolved and may have changed their parental environment. The outflow from the YSO and the accretion to the YSO therefore are the prime candidates for dissipating the dense cores.

5.2. *IRAS Color Temperature as an Evolutionary Indicator*

As discussed in the previous section, the 12 and 25 μm emission from the sources located inside L1641 (most of them are point sources) are probably the thermal emission from dust heated by the central sources. Since the color temperature $T[12, 25]$ is usually much higher than the color temperature obtained from longer wavelengths, $T[12, 25]$ measures the dust closer to the central embedded sources. Due to the large beam size of the *IRAS* telescope, $T[12, 25]$ is capable of sampling the dust with a scale of 10^{14} cm (equilibrium radius) for an *IRAS* source with a luminosity of 10 $L_\odot$.

Figure 5*b* displays the histograms of $T[12, 25]$ for the outflow sources, the T Tauri stars, and all other sources. As a group, the outflow sources are the coldest. The average $T[12, 25]$ of outflow sources is 137 K, compared with 180 K for all of the nonoutflow sources. The outflow sources appear to be much more deeply embedded in the dust shell than the pre–main-sequence stars, and their emergent flux is shifted to longer wavelengths.

5.3. *IRAS Luminosity as an Evolutionary Indicator*

Because the emission of the embedded sources is absorbed by the surrounding dust and reemitted at longer wavelengths, the far-infrared luminosity obtained in § 3.2 should account for most of the source luminosity. If we include the luminosity contribution at the shorter wavelengths (shorter than 5 μm), the luminosity would likely increase by a factor of no more than 2 Beichman et al. 1986). If disk reprocessing exists, the source luminosity may be overestimated by a factor of 2 (Wilking et al. 1989). Since the two corrections can compensate for each other, and we have no reliable information on either of them, it is assumed here that the luminosity derived in § 3.2 represents the source total luminosity within a factor of 2.

Figure 5*c* shows the luminosity histograms for detected outflows, T Tauri stars, and the other sources. It is clear that outflow sources tend to be more luminous than the nonoutflow sources. The average luminosity of outflow sources is 81 $L_\odot$, while that of the nonoutflows is only 7 $L_\odot$. There is no significant difference in the luminosity distribution of T Tauri stars and the other nonoutflow sources.

The greater luminosity of outflow sources has also been observed in other low-mass star-formation regions, such as Taurus (Myers et al. 1988) and ρ Oph (Wilking et al. 1989). There are three possible explanations: (1) this might be a selection effect in the sense that the CO outflow is easier to detect around the most luminous sources; (2) the outflow sources are more massive stars than the nonoutflow sources, and (3) the outflow sources are at a younger evolutionary stage and acquire significant luminosity from accretion or deuterium

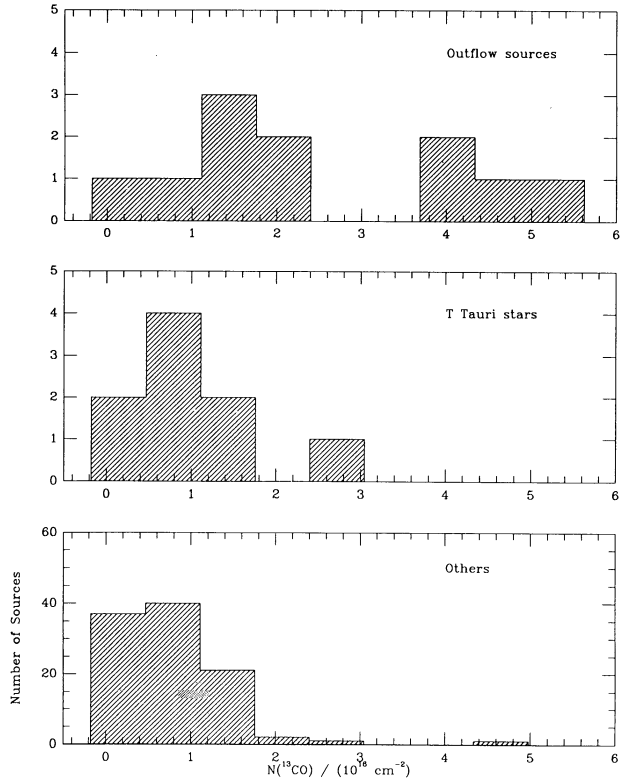

FIG. 5a

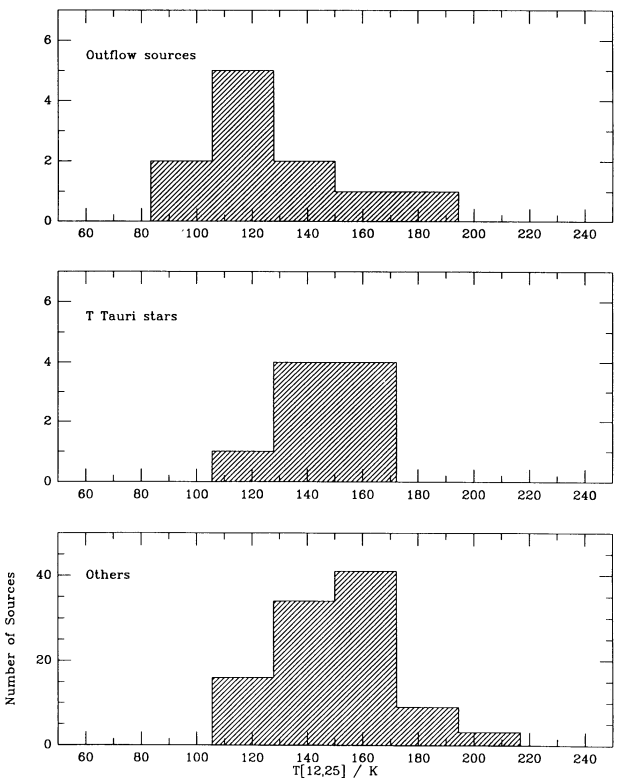

FIG. 5b

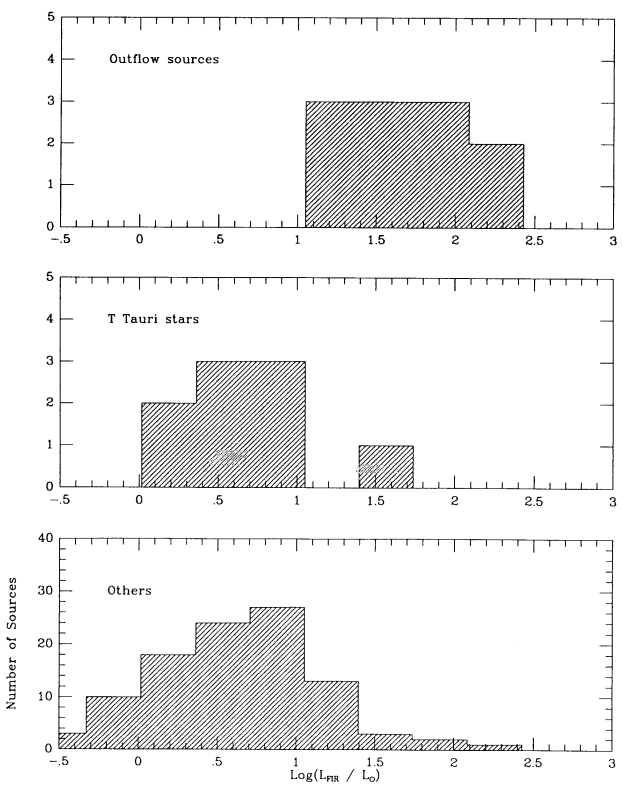

FIG. 5c

FIG. 5.—The histograms of (*a*) the ^{13}CO column density, (*b*) *IRAS* color temperature derived from the 12 and 25 μm flux ratio, and (*c*) luminosity of all the sources located inside L1641. Sources are shown in three groups: outflow sources, T Tauri stars, and all other sources.

burning. With the present data, we cannot conclusively discriminate among the possibilities; however, we favor (3) for the following reasons.

1. The unbiased Nagoya survey for CO outflow has a lower limit of 10^{-3} $L_\odot$ in mechanical luminosity. Using the correlation between the outflow mechanical luminosity and the star luminosity (Lada 1985), the survey should be capable of detecting any CO outflow from our *IRAS* source with luminosity greater than 1 $L_\odot$. Eight-five percent of our sources are brighter than that luminosity. Unless the outflow is smaller than the beam size of the Nagoya telescope (2.7), the outflow survey should be complete for 85% of the sources.

2. CO outflows have been detected around both high-mass and low-mass YSOs (Fukui 1989). It is unlikely that in L1641 only high-mass stars are associated with CO outflow.

3. L1641 is a low- and intermediate-mass star-formation region. The major young stellar population is believed to be T Tauri-type stars (Cohen & Kuhi 1979; Fukui 1989).

4. The average luminosity of the outflow sources is about 80 $L_\odot$. It can be easily accounted for if most of the YSO luminosity is obtained from the accretion. Since $L_{\rm acc} = GM\dot{M}R^{-1}$, a 1 $M_\odot$ star can have $L_{\rm acc} = 70$ $L_\odot$ for an accretion rate of 10^{-5} $M_\odot$ yr^{-1} and protostar radius of 4 $R_\odot$. The most luminous outflow source L1641 N has a luminosity of 220 $L_\odot$, and this could be the result of multiple heating sources of *IRAS* luminosity, as suggested by the near-IR images (Strom et al. 1989b; Chen et al. 1991, 1993).

We have also compared the luminosity distribution of the *IRAS* sources in L1641 with those in Ophiuchus and in Taurus-Auriga (Fig. 6). The data in Ophiuchus were taken from Wilking et al. (1989) and the data in Taurus were taken from Kenyon et al. (1990). Because L1641 is 3 times farther away from the Sun than both Ophiuchus and Taurus-Auriga,

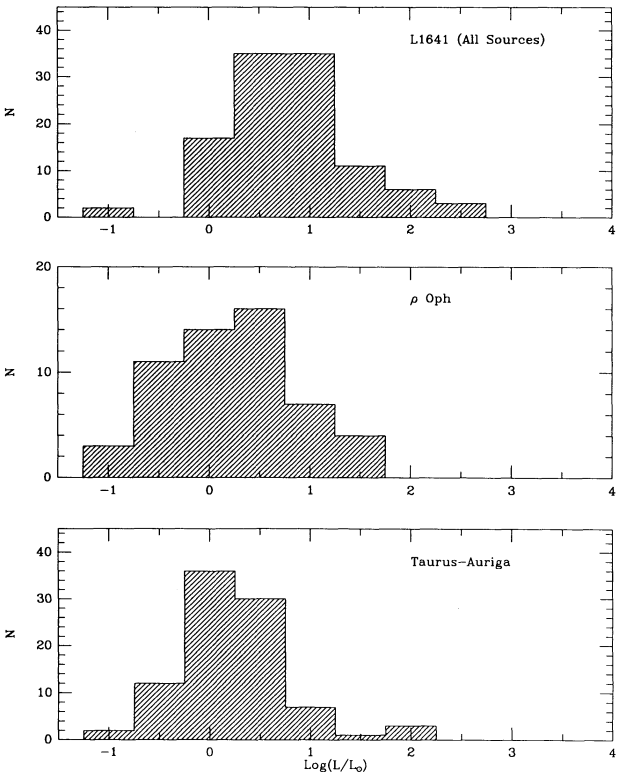

FIG. 6.—The luminosity distributions of *IRAS* sources in L1641 (all the sources inside molecular cloud), in ρ Oph (Wilking et al. 1989), and in Taurus-Auriga (Kenyon et al. 1990).

our detection limit is about 10 times higher. This explains the lack of low-luminosity objects ($L/L_\odot < 1$) in L1641. However, it is significant that there are more bright sources ($L/L_\odot > 10$) in L1641 than in the other two molecular clouds. One might attribute this difference to source confusion because the L1641 is 3 times farther away than the other two molecular clouds. A near-IR imaging of *IRAS* sources in L1641, however, suggests that source confusion may not be severe enough to drastically change the luminosity distribution in L1641 (Chen 1992; Chen & Tokunaga 1993). Of 59 *IRAS* sources imaged at 1–5 μm, 46 of them were identified as single sources. The different luminosity distributions can also be explained if the YSOs in L1641 are statistically more massive, or if the YSOs in L1641 are statistically younger. At present time, we cannot discriminate between these two possibilities.

TABLE 3

AVERAGE PHYSICAL PARAMETERS OF YSOs

Type	Number of Sources	L_{FIR} ($L_\odot$)	$N(^{13}CO)$ (10^{16} cm^{-2})	T[12, 25] (K)
Outflow sources	11	81.0	2.5	138
T Tauri stars	9	9.7	1.0	174
All other sources	107	6.4	0.7	181

6. SUMMARY

1. From *IRAS* co-added images, we have selected a flux-limited sample of 224 (98 point and 126 extended) sources in the star-forming region L1641.

2. The point sources and extended sources are significantly different. The point sources are associated with ^{13}CO molecular gas of L1641, while the extended sources are randomly distributed. They occupy different locations in the *IRAS* color-color diagram. We concluded that the sources inside L1641 (mostly point sources) are embedded YSOs, while the sources outside L1641 (mostly extended sources) are probably infrared cirrus heated by the interstellar radiation field.

3. By examining three physical parameters (T[12, 25], L_{FIR}, and $N[^{13}CO]$), we found that the outflow sources are significantly different from the nonoutflow sources (see Table 3). They are colder, more luminous, and are associated with higher column density. These differences can be explained if the outflow sources are embedded protostellar objects still in the accretion phase.

Further high-resolution observations are needed to define a more detailed evolutionary scheme similar to the H-R diagram for YSOs. This study provides an unbiased source sample in a single molecular cloud for future studies.

We sincerely thank the staff at IPAC for providing the *IRAS* co-added images and the addscan data, without which this work would never have been possible. We are also grateful to Gareth Wynn-Williams, George Herbig, and Klaus Hodapp for many helpful discussions, and to Ji Yang for his assistance during the ^{13}CO observations. H. C. was supported in part by a fellowship from the East-West Center, Honolulu, HI. A. T. T. and H. C. acknowledge the support of NASA grant NAGW-2278.

REFERENCES

Adams, F. C. 1990, ApJ, 363, 578
Bally, J., Langer, W. D., Stark, A. A., & Wilson, R. W. 1987, ApJ, 173, 324
Beichman, C. A. 1985, in Light on Dark Matter, ed. F. P. Israel (Dordrecht: Reidel), 279
Beichman, C. A., Neugebauer, G., Habing, H. J., Clegg, P. E., & Chester, T. J., ed. 1988, Infrared Astronomical Satellite Catalogs and Atlases, Vol. 1, Explanatory Supplement (Washington, DC: GPO)
Beichman, C. A., Myers, P. C., Emerson, J. P., Harris, S., Mathieu, R., Benson, P. J., & Jennings, R. E. 1986, ApJ, 307, 337
Boulanger, F., Beichman, C. A., Desert, J. P., Helou, G., Perault, M., & Ryter, C. 1988, ApJ, 333, 328
Chen, H. 1992, Ph.D. thesis, Univ. Hawaii
Chen, H., Fukui, Y., & Iwata, T. 1993, ApJ, in press (July 15)
Chen, H., Fukui, Y., & Yang, J. 1992, ApJ, 398, 544
Chen, H., & Tokunaga, A. T. 1993, ApJS, submitted
Chen, H., Tokunaga, A. T., & Hodapp, K.-W. 1991, Mem. Soc. Astron. Ital., 62, 737
Chen, H., Tokunaga, A. T., Strom, K. M., & Hodapp, K.-W. 1993, ApJ, 407, 637
Cohen, M., & Kuhi, L. O. 1979, ApJS, 41, 743
Dickman, R. L., & Herbst, W. 1990, ApJ, 357, 531
Draine, B. T., & Lee, H. M. 1984, ApJ, 285, 494
Emerson, J. P. 1988a, in Formation and Evolution of Low Mass Stars, ed. A. K. Dupree & M. T. V. T. Lago (Dordrecht: Kluwer), 21
———. 1988b, in Formation and Evolution of Low Mass Stars, ed. A. K. Dupree & M. T. V. T. Lago (Dordrecht: Kluwer), 193
Fukui, Y. 1989, in Low Mass Star Formation and Pre–Main-Sequence Objects, ed. B. Reipurth (Garching: ESO), 95
Fukui, Y., Iwata, T., Takaba, H., Mizuno, A., Ogawa, H., Kawabata, K., & Sugitani, K. 1989, Nature, 342, 161
Fukui, Y., & Mizuno, A. 1991, in IAU Symp. 147, Fragmentation of Molecular Clouds and Star Formation, ed. E. Falgarone, F. Boulanger, & G. Duvert (Dordrecht: Kluwer), 275
Fukui, Y., Sugitani, K., Takaba, H., Iwata, T., Mizuno, A., Ogawa, H., & Kawabata, K. 1986, ApJ, 311, L85
Herbig, G. H., & Bell, K. R. 1988, Lick Obs. Bull., No. 1111
IRAS Point Source Catalog, 1988, Joint *IRAS* Science Working Group (Washington, DC: GPO) (PSC)

Keynon, S. J., Hartmann, L. W., Strom, K. M., & Strom, S. E. 1990, AJ, 99, 869
Lada, C. J. 1985, ARA&A, 23, 267
Lynds, B. T. 1962, ApJS, 7, 1
Morgan, J., & Bally, J. 1991, ApJ, 372, 505 (MB)
Morgan, J., Schoerb, F. P., Snell, R. L., & Bally, J. 1991, ApJ, 376, 618
Morgan, J., Snell, R. L., & Strom, K. M. 1990, ApJ, 362, 274
Myers, P. C., & Benson, P. J. 1983, ApJ, 266, 309
Myers, P. C., Fuller, G. A., Mathieu, R. D., Beichman, C. A., Benson, P. J., Schild, R. E., & Emerson, J. P. 1987, ApJ, 319, 340
Myers, P. C., Heyer, M., Snell, R., & Goldsmith, P. F. 1988, ApJ, 324, 908
Schwartz, R. D., Gyuludaghian, A. L., & Wilking, B. A. 1991, ApJ, 370, 263
Scoville, N. Z., Sargent, A. I., Sanders, D. B., Claussen, M. J., Masson, C. R., Lo, K. Y., & Philips, T. G. 1986, ApJ, 303, 416
Selgren, K. 1985, ApJ, 277, 623
Strom, K. M., Margulis, M., & Strom, S. E. 1989a, ApJ, 345, L79
Strom, K. M., Newton, G., Strom, S. E., Seaman, R. L., Carrasco, L., Cruz-Gonzalez, I., Serrano, A., & Grasdalen, G. 1989b, ApJS, 71, 183
Strom, K. M., et al. 1990, ApJ, 362, 168
Wilking, B. A., Lada, C. J., & Young, E. T. 1989, ApJ, 340, 823